

Mitigating transients in flux-control signals in a superconducting quantum processor

Anuj Aggarwal,¹ Jorge Fernández-Pendás,¹ Tahereh Abad,¹ Daryoush Shiri,¹ Halldór Jakobsson,¹ Marcus Rommel,¹ Andreas Nylander,¹ Emil Hogedal,¹ Amr Osman,¹ Janka Biznárová,¹ Robert Rehammar,¹ Michele Faucci Giannelli,¹ Anita Fadavi Roudsari,¹ Jonas Bylander,¹ and Giovanna Tancredi¹

Department of Microtechnology and Nanoscience, Chalmers University of Technology, SE-412 96 Gothenburg, Sweden

(*Electronic mail: tancredi@chalmers.se)

(Dated: 12 March 2025)

Flux-tunable qubits and couplers are common components in superconducting quantum processors. However, dynamically controlling these elements via current pulses poses challenges due to distortions and transients in the propagating signals. In particular, long-time transients can persist, adversely affecting subsequent qubit control operations. We model the flux control line as a first-order RC circuit and introduce a class of pulses designed to mitigate long-time transients. We theoretically demonstrate the robustness of these pulses against parameter mischaracterization and provide experimental evidence of their effectiveness in mitigating transients when applied to a flux-tunable qubit coupler. The proposed pulse design offers a practical solution for mitigating long-time transients, enabling efficient and reliable experiment tune-ups without requiring detailed flux line characterization.

I. INTRODUCTION

Superconducting quantum processors have emerged as one of the leading platforms for the physical realization of quantum computers because of their scalability and performance^{1–6}. The majority of superconducting processors utilize flux-tunable qubits or flux-tunable couplers to implement two-qubit gates^{7–11}, reset operations^{12,13} and leakage reduction schemes^{14–16} by varying the transition frequency of the tunable element statically and/or dynamically. Precise flux control is a requirement to further improve the fidelity of quantum operations and advance the state of the art.

Flux-tunable elements on a processor are typically inductively coupled to flux control lines, often referred to as Z-lines. These control lines consist of a series of coaxial cables, attenuators, filters, and a bias-tee (see Fig. 1 (a–b)). While applying a con-

stant current is straightforward, achieving the desired dynamic control is cumbersome. This is due to pulse distortions, caused by impedance mismatches and transients arising from capacitors and inductors. A primary solution to compensate for distortion (or transients) is to use a predistortion technique, i.e., one finds the transfer function $h(t)$ of the entire flux control line and applies its inverse $h^{-1}(t)$. However, because most of the components are at cryogenic temperatures, the transfer function needs to be measured using the flux-tunable element on-chip. While several methods have been proposed for characterizing the transfer function of flux pulses on-chip^{17–28}, this is complex and time-consuming, posing a potential challenge when scaling up the number of qubits.

In our system, distortions of the flux control pulse can be categorized as short-time effects (≤ 100 ns) and long-time effects (≥ 1 μ s). Short-time effects occur on the timescale of a single flux pulse op-

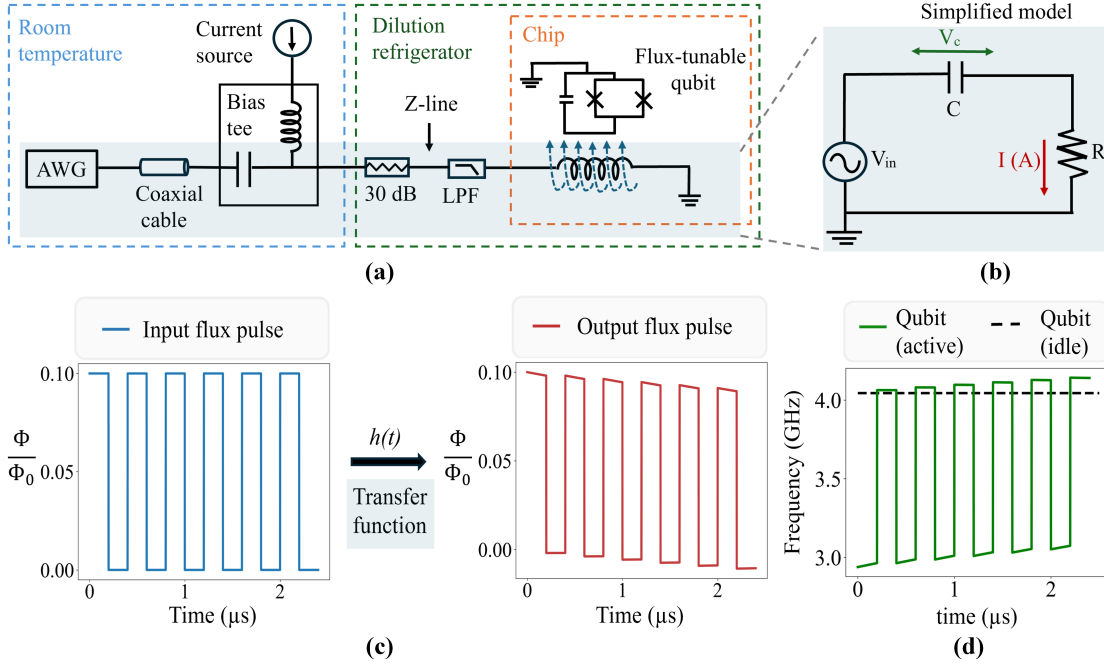


FIG. 1. (a) Circuit schematic of a typical flux (Z) control line. An arbitrary waveform generator (AWG) is used to send arbitrary flux pulses via a bias-tee. The attenuators and low-pass filter are used to reduce noise. The flux line is terminated on chip and is used to control the frequency of a flux-tunable qubit or coupler. (b) Simplified first-order RC model of the flux control line to account for the transients. The bias tee constitutes the dominant contribution to the capacitance C while attenuators contribute to resistance R . (c) Example demonstration of long-timescale transients using the simplified model showing how the input flux pulse is deformed by the transfer function $h(t)$ of the flux control line, assuming a decay time constant $\tau = 10 \mu s$. (d) Illustration of the impact of transients on the frequency of a tunable qubit, assuming $\omega_{max}/2\pi = 5$ GHz and an idle flux bias $\Phi = 0.2 \Phi_0$. The figure highlights the non-repeatability of qubit's frequency changes and the failure of the qubit to return to its idling point, which adversely affects subsequent qubit operations.

eration, and can arise from impedance mismatching and overshoot from inductive and capacitive elements in the flux control line. Long-time effects persist much longer than the duration of the pulse and degrade subsequent operations such as single- and two-qubit gates. They are dominated by high-pass filtering from resistive and capacitive elements in the wiring. Figure 1(c) shows an example of flux-pulse deformation due to long-time transients arising from the flux control line, assuming a decay constant τ of $10 \mu s$. The impact of these transients on the frequency of a tunable qubit, with $\omega_{max}/2\pi = 5$ GHz, is illustrated in Fig. 1(d). Digi-

tal filters are typically employed^{19,29} to compensate for these distortions. Although it has been demonstrated that they can be corrected, we are not aware of any simple analytical model of the flux control wiring to guide the design of flux control pulses.

In this paper, we propose a simple yet effective model for capturing long-time distortions in a typical flux-line setup, based on a first-order series RC circuit. This allows us to find a class of flux pulses that are resilient to first-order RC transients, providing a simple and robust solution with minimal calibration. We focus on the application of flux

pulses that are non-modulated and low in frequency, which are typically used to dynamically adjust flux-tunable elements. In particular, we apply our findings to control the coupler in a two-qubit quantum processor and demonstrate, with minimal calibration, that the applied flux pulse is resilient to transients. We show that the proposed transient mitigation technique is robust against mischaracterization of the effective model parameters.

The paper is organized as follows. In Section II, we describe the measurement scheme for characterizing flux transients. In Section III, we present a theoretical model that establishes the conditions for generating transient-free pulses in a flux control line dominated by a series RC circuit. In Section IV, we examine the robustness of the method against mischaracterization of the transient decay constant. In Section V, we discuss the class of net-zero pulses, and we conclude the paper in Section VI.

II. MEASURED TRANSIENTS

We start by characterizing the flux transients in our experimental setup. The device is shown in Fig. 2(a); it consists of two fixed-frequency transmon qubits³¹ (Q1 and Q2), coupled via a flux-tunable coupler^{32,33}. Both qubits have dedicated readout resonators and XY microwave drive lines, while the coupler has only a flux control line (Z-line). This Z-line controls the flux threading the coupler's SQUID (superconducting quantum interference device), enabling the tuning of the coupler's frequency.

When the coupler is biased near the qubit frequency, any variation in the coupler's frequency causes a shift of the transition frequency of the coupled qubit. Since there is no readout resonator on the coupler, we employ qubit Q1 as a probe to sense the transients in the flux control signal. To achieve high sensitivity, we bias the coupler in an avoided-crossing region with Q1, where qubit and coupler hybridize.

We use Ramsey interference of the qubit to

measure the transient characteristics of the flux line^{10,17,18,34}. Figure 2(b) shows the experimental procedure: two $\pi/2$ pulses are applied to qubit Q1, and a square-shaped flux pulse of duration $\tau_{\text{pulse}} = 8 \mu\text{s}$ to the coupler, which causes a dispersive shift of the qubit frequency. The qubit expectation values $\langle X \rangle$ and $\langle Y \rangle$ are measured as a function of the delay time τ_{delay} . In a system with no transients, there are no oscillations in $\langle X \rangle$ and $\langle Y \rangle$ as the qubit frequency is not shifted away from its nominal value during the delay time period when the flux pulse is off. However, we measure oscillations in the expectation values, as shown in Fig. 2(c). The phasor representation of the expectation values as a function of τ_{delay} is shown in Fig. 2(d). Taking the inverse tangent of $\langle Y \rangle / \langle X \rangle$, we extract how the unwrapped qubit phase changes with τ_{delay} , see Fig. 2(e). The derivative of the phase is then used to extract the change in qubit frequency as a function of τ_{delay} , as shown in Fig. 2(f). To translate the frequency changes into flux variations, we performed qubit spectroscopy as a function of flux (Fig. 2(g)). We then convert the frequency to flux and fit the transients with an exponentially decaying function, $A(-e^{-\tau_{\text{delay}}/\tau} + e^{-(\tau_{\text{delay}} + \tau_{\text{pulse}})/\tau}) + B$, which is an approximation of the measured response. We find $\tau = 13 \mu\text{s}$, as shown in Fig. 2(h). We identify this time constant with the characteristic time constant of the RC circuit, which is discussed in the next section. We note that although exponential decay captures most of the transient behavior, there exist some long-term effects (measured up to 300 μs) that are shown in Fig. 6 of the Appendix.

III. ANALYTICAL MODEL OF TRANSIENT-FREE PULSES

We model the flux control line as a first-order series RC circuit as shown in Fig. 1(b). This is a valid assumption for the case of pulses that are non-modulated and low in frequency, often referred to as DC flux pulses. Typically, these pulses have a duration $\tau_{\text{pulse}} \geq 50 \text{ ns}$, corresponding to a frequency $\leq 20 \text{ MHz}$. If we consider a net contribution of 2 nH arising from wire bonds³⁵ and the Z-line coplanar

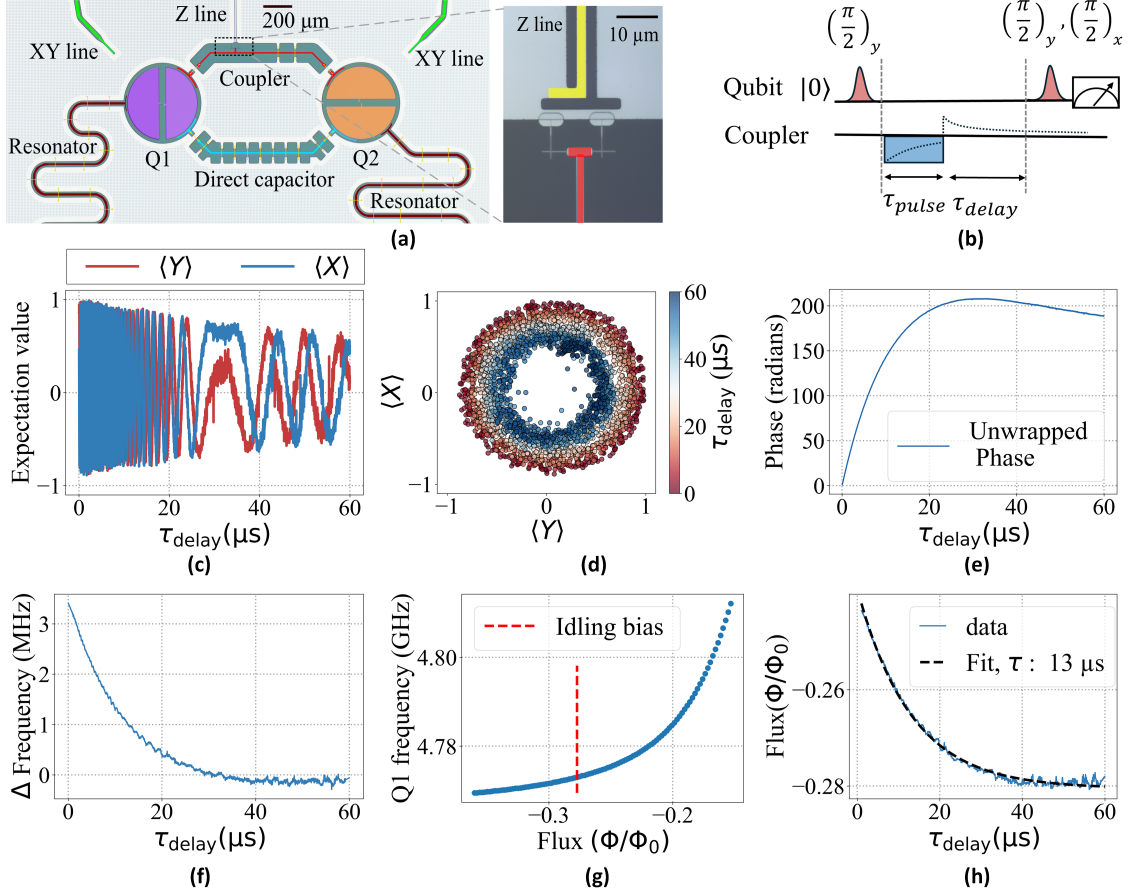


FIG. 2. Measuring flux transients. (a) Device micrograph with false coloring: two fixed-frequency qubits and one flux tunable coupler. The right-hand side image shows a zoomed-in view of the Z-line (yellow), shorted to ground, inductively coupled to the SQUID loop of the coupler. (b) Ramsey interference pulse scheme to measure flux transients in the absence of direct readout of the coupler. We fix the coupler pulse length τ_{pulse} and vary the delay τ_{delay} while measuring the qubit's expectation values $\langle X \rangle$ and $\langle Y \rangle$. (c) Quadratures $\langle X \rangle$ (blue) and $\langle Y \rangle$ (red) as a function of τ_{delay} for qubit Q1. The observed oscillations indicate the presence of transients. (d) Phasor plot of $\langle X \rangle$ and $\langle Y \rangle$ as a function of τ_{delay} . (e) Extracted unwrapped phase from the inverse tangent of $\langle Y \rangle / \langle X \rangle$. The unwrapped phase is also filtered using the Savitzky-Golay method³⁰ to reduce high-frequency noise. (f) Extracted change in qubit frequency as a function of time. (g) Mapping between the frequency of qubit Q1 and the normalized flux, with the idling bias shown by the red-dashed line. (h) Extracted flux fitted with a decaying exponential function, showing a decay time constant $\tau = 13 \mu\text{s}$.

waveguide³⁶, we get $\omega L \approx 2\pi \times 20 \text{ MHz} \times 2 \text{ nH} \approx 0.25 \Omega$. This allows us to neglect the inductive contribution in this frequency range.

In our model, given an input signal $V_{\text{in}}(t)$ and a

voltage drop $V_c(t)$ across the capacitor, we can write

$$\tau \frac{dV_c(t)}{dt} + V_c(t) = V_{\text{in}}(t), \quad (1)$$

where $\tau = RC$. We assume that $V_{\text{in}}(t)$ has a general

Condition I	$\sum_{n=0}^N a_n = 0$	The input signal V_{in} begins and ends at zero.
Condition II	$k_{\text{exp}} = a_0 + \sum_{n=1}^N \frac{a_n - n\omega\tau b_n}{1 + (n\omega\tau)^2} = 0$	Transient cancellation.
Condition III	$\sum_{n=1}^N n \frac{n\omega\tau a_n + b_n}{1 + (n\omega\tau)^2} = 0$	The current/flux pulse begins and ends at zero.

TABLE I. Conditions for smooth, transient-free pulses.

sine-cosine Fourier series form

$$V_{in}(t) = a_0 + \sum_{n=1}^N [a_n \cos(n\omega t) + b_n \sin(n\omega t)], \quad (2)$$

with $\omega = 2\pi/\tau_{\text{pulse}}$ and index n referring to the n^{th} harmonic. We solve Eq. (1) and find the voltage across the capacitor $V_c(t)$ for any arbitrary V_{in} :

$$\begin{aligned} V_c(t) = & a_0 - \left[a_0 + \sum_{n=1}^N \frac{a_n - n\omega\tau b_n}{1 + (n\omega\tau)^2} \right] e^{-\frac{t}{\tau}} \\ & + \sum_{n=1}^N \frac{a_n - n\omega\tau b_n}{1 + (n\omega\tau)^2} \cos(n\omega t) \\ & + \sum_{n=1}^N \frac{n\omega\tau a_n + b_n}{1 + (n\omega\tau)^2} \sin(n\omega t). \end{aligned} \quad (3)$$

As a result, the current flowing in the circuit, which generates the magnetic flux and thereby adjusts the tunable element's frequency, is

$$\begin{aligned} I(t) = & C \frac{dV_c(t)}{dt} \\ = & \frac{1}{R} \left[a_0 + \sum_{n=1}^N \frac{a_n - n\omega\tau b_n}{1 + (n\omega\tau)^2} \right] e^{-\frac{t}{\tau}} \\ & - C\omega \sum_{n=1}^N n \frac{a_n - n\omega\tau b_n}{1 + (n\omega\tau)^2} \sin(n\omega t) \\ & + C\omega \sum_{n=1}^N n \frac{n\omega\tau a_n + b_n}{1 + (n\omega\tau)^2} \cos(n\omega t). \end{aligned} \quad (4)$$

Equation (4) shows that the current has two types of oscillating terms and an exponential decaying term. The latter is responsible for the appearance of transients, and the sum in the square brackets will be referred to as k_{exp} .

In principle, we have arbitrary control over the input flux pulse V_{in} as we can choose any values for the coefficients of cosine terms (a_n), sine terms (b_n), and the DC offset (a_0). However, we need to impose three conditions to generate a physical signal that does not produce either jumps or transients. First of all, the sum of the cosine coefficients and the DC offset must be zero (Condition I): V_{in} has to start and end at zero. Secondly, to cancel the transient, the coefficient of the exponential term in Eq. (4) must be equal to zero (Condition II). Lastly, the sum of cosine terms in the current (resulting flux) in Eq. (4) must be zero (Condition III), such that the flux that reaches the tunable element starts and ends at zero. These conditions are summarized in Table I. Note that although a_0 can be used, it is hard to calibrate it in practice. Considering these three conditions, and setting $a_0 = 0$, limit our freedom in terms of arbitrary pulses.

IV. ROBUSTNESS AGAINST RC-CONSTANT MISCHARACTERIZATION

Assuming one knows τ and chooses a V_{in} that satisfies the three conditions in Table I, a transient-free control pulse can be achieved. Here, we analyze k_{exp} and determine whether an accurate characterization of τ is needed. Focusing on simple example cases, we showcase our theoretical findings and compare them with our experimental results.

A. Theoretical analysis

To study the robustness of the method when the time constant τ is mischaracterized, we solve Condition II by substituting ' τ ' with ' $m\tau$ ', where m is the estimation factor. One possible strategy to design V_{in} is to use the N^{th} harmonic coefficients to cancel the contribution of the other $N - 1$ harmonics in the coefficient k_{exp} . Under this change of parameters and separation of coefficients, Condition II becomes:

$$a_0 + \sum_{n=1}^{N-1} \frac{a_n - n\omega m \tau b_n}{1 + (n\omega m \tau)^2} + \frac{a_N - N\omega m \tau b_N}{1 + (N\omega m \tau)^2} = 0. \quad (5)$$

From Eq. (5), one can extract the coefficients a_N and b_N . Since τ is mischaracterized, these values would be incorrect for perfect cancellation of k_{exp} . The non-zero k_{exp} can then be calculated as

$$k_{exp} = a_0 + \sum_{n=1}^{N-1} \frac{a_n - n\omega \tau b_n}{1 + (n\omega \tau)^2} + \frac{a_N - N\omega \tau b_N}{1 + (N\omega \tau)^2}. \quad (6)$$

To gain an analytical understanding of cases where τ is highly overestimated, we calculate k_{exp} for $m \gg 1$ in the case of V_{in} containing either sine-only terms or cosine-only terms. We focus on a practical case where the flux pulse duration is shorter than the decay time constant τ , i.e., $\omega\tau > 1$ and $a_0 = 0$. Considering only the dominant terms gives:

$$k_{exp}^{cos} = \sum_{n=1}^{N-1} \frac{a_n}{1 + (n\omega \tau)^2} + \frac{-N^2}{1 + (N\omega \tau)^2} \sum_{n=1}^{N-1} \frac{a_n}{n^2}, \quad (7)$$

$$k_{exp}^{sin} = \sum_{n=1}^{N-1} \frac{-n\omega \tau b_n}{1 + (n\omega \tau)^2} + \frac{N^2 \omega \tau}{1 + (N\omega \tau)^2} \sum_{n=1}^{N-1} \frac{b_n}{n} \quad (8)$$

for cosine-only and sine-only V_{in} , respectively. Looking at Eqs. (7) and (8), it is clear that when $\omega\tau$ becomes much greater than 1, the denominator can be further simplified, and both k_{exp}^{cos} and k_{exp}^{sin} tend to zero, leading to the suppression of transients.

To quantitatively evaluate the effectiveness of the method, we take a simple example of a bi-harmonic sine signal,

$$V_{in}(t) = b_1 \sin(\omega t) + b_2 \sin(2\omega t). \quad (9)$$

Here, Condition I is already satisfied as there are no cosine terms, and Condition II and Condition III are equivalent. If one knows the time constant τ , full transient cancellation is achieved when Condition II is satisfied. In this case, one gets

$$k_{exp} = \frac{-b_1 \omega \tau}{1 + (\omega \tau)^2} + \frac{-2b_2 \omega \tau}{1 + (2\omega \tau)^2}. \quad (10)$$

Imposing $k_{exp} = 0$ gives a relation between the coefficients b_1 and b_2 :

$$b_2 = \frac{-b_1}{2} \frac{1 + (2\omega \tau)^2}{1 + (\omega \tau)^2}. \quad (11)$$

If τ is not well known, one can replace τ with $m\tau$, and Eq.(11) becomes

$$b_2 = \frac{-b_1}{2} \frac{1 + (2\omega m \tau)^2}{1 + (\omega m \tau)^2}. \quad (12)$$

Figure 3(a) shows k_{exp} , Eq. 10, as a function of m and $\omega\tau$ when we set $b_1 = 1$ and b_2 is given by Eq. (12). It is interesting to note that for large and small $\omega\tau$, k_{exp} is small despite the large variation in m . For $\omega\tau$ close to one, there is instead a significant error from the mischaracterization of τ . Figure 3(b) shows the exponential coefficient k_{exp} as a function of m for $\omega\tau = 8.79$ rad, which we use in measurements presented later. It can be seen that for large values of m , k_{exp} is negligibly small and therefore the overestimation of τ still leads to a significant suppression of first-order RC transients. To understand this suppression of transients, we simplify Eq. (12) for $m \gg 1$ and get

$$b_2 \approx -2b_1. \quad (13)$$

We can now write k_{exp} as

$$k_{exp} = \frac{3b_1 \omega \tau}{1 + 5\omega^2 \tau^2 + 4\omega^4 \tau^4}, \quad (14)$$

which for $\omega\tau \gg 1$ becomes

$$k_{exp} \approx \frac{3b_1}{4\omega^3 \tau^3}. \quad (15)$$

It is interesting to compare the coefficient k_{exp} in Eq. (15) to what would be obtained in the case of

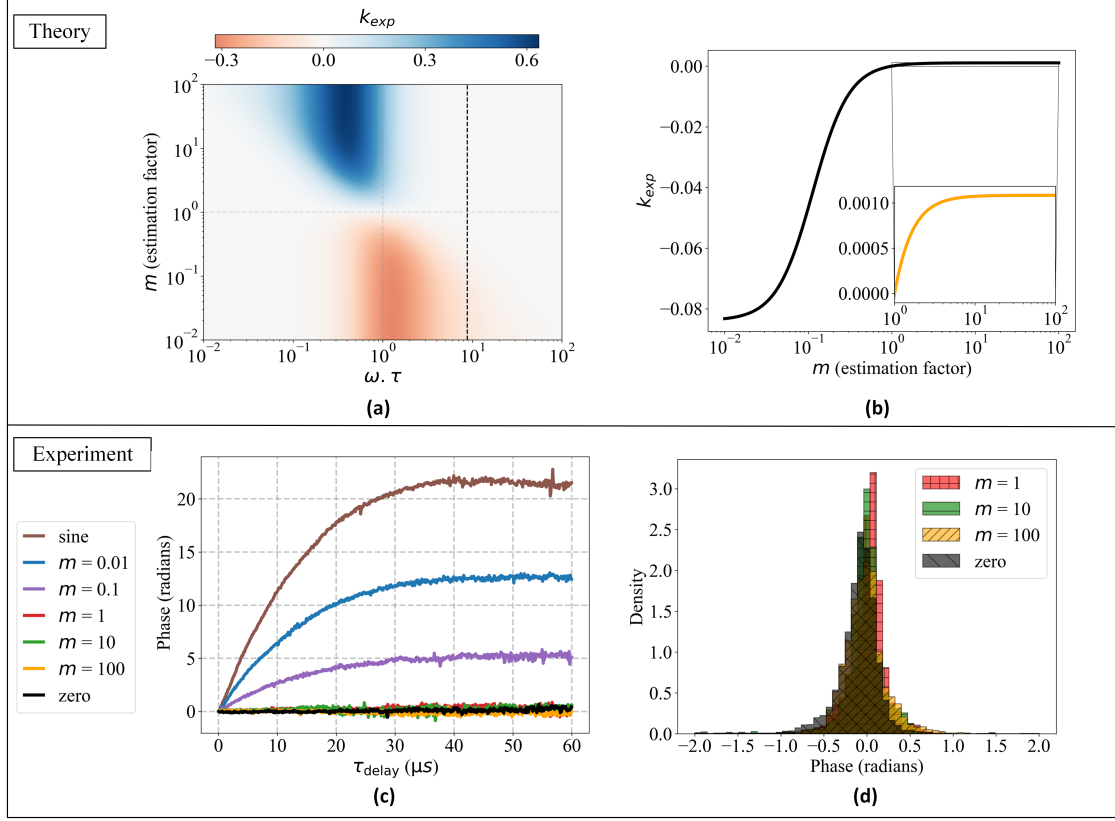


FIG. 3. Robustness of the method investigated using the example case of a bi-harmonic sine signals, $V_{in} = b_1 \sin(\omega t) + b_2 \sin(2\omega t)$, with $\tau = 11.2 \mu\text{s}$. (a) Analytical calculation of k_{exp} as a function of $\omega\tau$ and m given by Eqs. (10) and (12). Here m is the estimation factor of τ , such that the decay constant τ is mischaracterized as $m\tau$. The dashed line shows the $\omega\tau$ value used in measurements. (b) Line-cut along the dashed line in (a), demonstrating that the overestimation of τ preserves the mitigation of transients. (c) Experimental verification: Acquired phase by qubit Q1 as a function of τ_{delay} , extracted via the Ramsey-like method in Fig. 2(a) for different pulse shapes: zero (reference pulse), single-frequency pulse V_{in} (sine), and bi-harmonic pulse V_{in} for different values of the estimation factor m . The values $m = 10$ (green) and 100 (orange) indicate over-estimation while $m = 0.1$ (purple) and 0.01 (blue) represent under-estimation, and $m = 1$ shows the exact value of τ used for the bi-harmonic pulse. The single-frequency pulse V_{in} (brown) results in the highest acquired phase, thus representing greater transients. (d) Histograms of the acquired phase for $m = 1, 10, 100$, and the reference pulse (zero). Each histogram consists of 11 sets of measurements of each pulse type, excluding some measurements with coherence time below $30 \mu\text{s}$. Note that the $\tau = 11.2 \mu\text{s}$ used in this experiment is slightly different from the one estimated in Fig. 2(h) ($\tau = 13 \mu\text{s}$); this discrepancy is due to parameter extraction with a refined fitting method at a later stage.

a single-frequency sine signal, $V_{in} = b_1 \sin(\omega t)$. In this case, the coefficient of the transient would be $k_{\text{exp}} = -b_1/\omega\tau$. Although we are comparing two different pulse shapes, this still provides insight; for $\omega\tau \gg 1$, an overestimation of the time constant pro-

vides a stronger suppression of transients for a bi-harmonic sine signal in comparison to a standard single-frequency pulse shape.

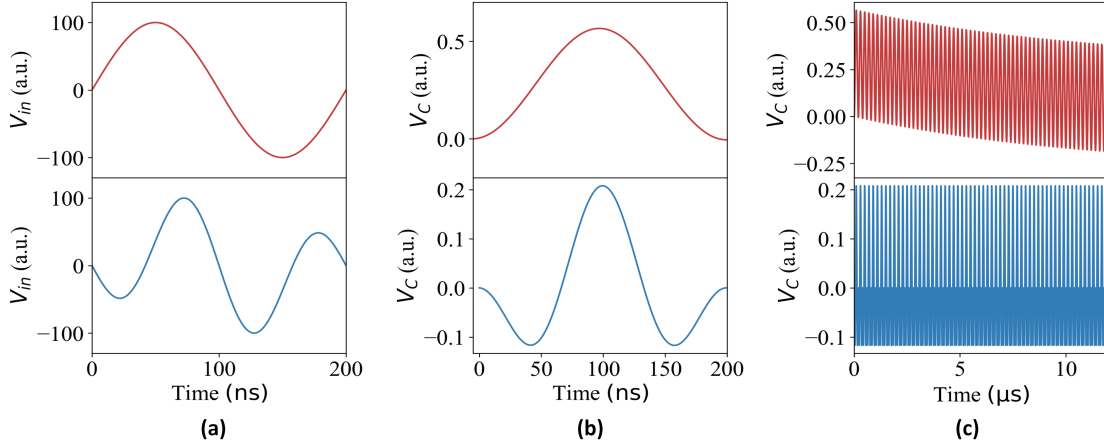


FIG. 4. Comparison between using either a single-frequency sine signal (red curve) or a bi-harmonic sine signal (blue curve), highly overestimating the time constant with $b_2 = -2 b_1$. We consider that the system has an RC time constant $\tau = 11.2 \mu\text{s}$. (a) Input pulse shape $V_{in}(t)$ for one period. (b) Capacitor response $V_C(t)$ for one period. (c) Capacitor response $V_C(t)$ over multiple periods. The resulting $V_C(t)$ in the case of the single-frequency sine signal has transients, while in the case of the bi-harmonic sine signal transients are almost negligible.

B. Experimental verification

We experimentally verify the robustness of our technique using the bi-harmonic sine signal, $V_{in} = b_1 \sin(\omega t) + b_2 \sin(2\omega t)$, discussed earlier. We characterize the transients using the method outlined in Section II. The acquired phase after the flux pulse is treated as the figure of merit for the transients. The acquired phase refers to the subtracted phase offset from the extracted unwrapped phase. We measure the acquired phase as a function of τ_{delay} for a variety of pulses of length $\tau_{\text{pulse}} = 8 \mu\text{s}$: a zero-amplitude pulse for reference, a sinusoidal pulse, and bi-harmonic sine pulses with different values of the estimation factor m .

The results are shown in Fig. 3(c), demonstrating that an overestimation of the time constant leads to negligible transients. The measured phases for $m = 10$ and 100 almost overlap with those for $m = 1$ and the zero pulse. Note that, as predicted by the theory, underestimating τ leads to increased transients as shown for $m = 0.1$ and 0.01 (see Fig. 3(b)). Interestingly, our measurement shows that a single-

frequency sine pulse results in even larger transients.

To further investigate the cases in which we overestimate the time constant, we repeated the evaluation of the phase 11 times, for $m = 1, 10, 100$, and the reference case (zero pulse). Figure 3(d) shows the resulting histogram plot of the acquired phase. It is clear that an overestimation of the time constant in the bi-harmonic sine pulse causes transients that are almost equivalent to that of the zero pulse case (reference).

V. DISCUSSION OF NET-ZERO PULSES

Net-zero (NZ) pulses are typically used for flux pulses because they exhibit reduced long-timescale transient effects. They are defined as bipolar pulses with zero net area, resulting in no DC component⁸. In our experiment, we tested input signals having the form of single frequency and bi-harmonic sine pulses (see Fig. 3(c)). We show that, while both pulses fall within the category of net-zero, they pro-

duce different transients.

To understand this discrepancy, we compare the voltage drop $V_c(t)$ across the capacitor³⁷ (see Fig. 4(b)). $V_c(t)$ for the bi-harmonic sine pulse is (approximately) net zero, while it is not net-zero for the single-frequency sine pulse. In Fig. 4(c), we compare the capacitor’s response over multiple periods showing that $V_c(t)$ for the single-frequency sine signal has significant transients in comparison to the bi-harmonic case. This elucidates that the net-zero nature of the input pulse is not a sufficient condition to minimize RC transients. For effective suppression of transients, the capacitor’s response $V_c(t)$ should also be net zero.

VI. CONCLUSION

In this work, we present a simple analytical model that captures dominant long-timescale transients in a typical flux control line. We introduce a class of flux control pulses designed to mitigate these transients and provide both theoretical analysis and experimental validation of their effectiveness. Furthermore, we demonstrate the robustness of this approach against mischaracterization of model parameters, enabling efficient experiment tune-ups without detailed transient characterization. We believe that the proposed method provides a practical solution for improving flux control in superconducting quantum processors.

VII. ACKNOWLEDGMENTS

We would like to thank Simon Pettersson Fors, Christopher W. Warren, Tomas McKelvey, and Per Delsing for useful discussions. This research was financially supported by the Knut and Alice Wallenberg Foundation through the Wallenberg Center for Quantum Technology (WACQT) and by the EU Flagship on Quantum Technology HORIZON-CL4-2022-QUANTUM-01-SGA project 101113946 OpenSuperQPlus100. The fab-

rication of our quantum processor was performed at Myfab Chalmers.

VIII. DATA AVAILABILITY

See the Appendix for theoretical and experimental details. All relevant data and figures supporting the main conclusions of the document are available on Zenodo. Please refer to Anuj Aggarwal at anuja@chalmers.se if needed.

Appendix A: Measurement setup

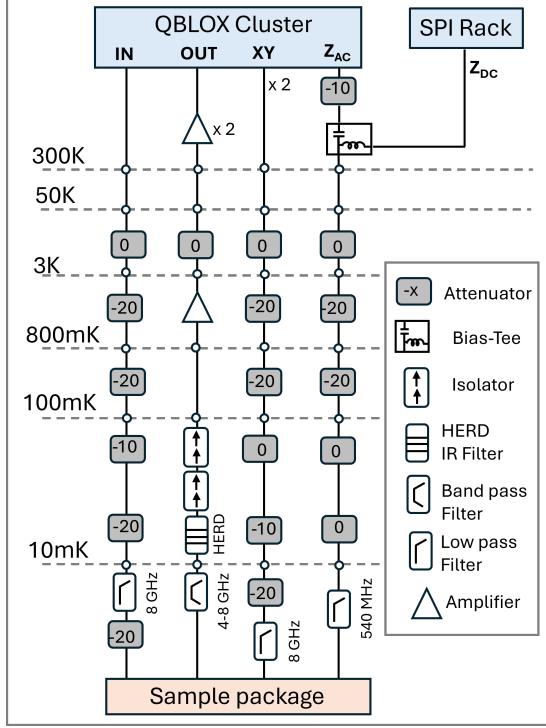


FIG. 5. Schematic diagram of the measurement setup. The control lines are defined as follows: XY - qubit microwave drive line, IN - readout input line, and OUT - readout output line. Z_{AC} (dynamic) and Z_{DC} (static) flux control lines are coupled via a bias-tee at room temperature. Attenuator values are specified in dB units. HERD is an IR blocking filter, see Ref.³⁸

The schematic diagram of the measurement setup is shown in Fig. 5. The device is mounted at the 10 mK stage of a Bluefors LD250 dilution refrigerator. The quantum processor consists of two floating transmon qubits coupled via a coupler (frequency-tunable transmon). Each qubit is coupled to individual readout (quarter-wavelength) resonators and microwave drive lines. The coupler has a SQUID which is inductively coupled to a flux control line. The coupler does not have its own dedicated readout resonator. In the experiments, we use qubit Q1 to measure flux pulse transients. The parameters of

qubit Q1 and the coupler are listed in Table II.

Parameter		Q1
Qubit frequency	$\omega_q/2\pi$ (GHz)	4.7730
Qubit anharmonicity	$\alpha/2\pi$ (MHz)	-236
Resonator frequency	$\omega_r/2\pi$ (GHz)	6.99757
Resonator linewidth	$\kappa_r/2\pi$ (kHz)	409
Relaxation time	T_1 (μ s)	78
Decoherence time	T_2^* (μ s)	75
Coupler freq. ($\Phi = 0$)	$\omega_c/2\pi$ (GHz)	4.8575
Qubit-coupler coupling	$g/2\pi$ (MHz)	63

TABLE II. Qubit Q1 parameters and coherence properties at a coupler flux bias $\Phi = -0.278 \Phi_0$.

The device is fabricated on a highly resistive silicon substrate. After chemical cleaning, an aluminum ground layer is deposited, and the device pattern, excluding Josephson junctions and air bridges, is defined via optical lithography, followed by etching to form resonators, the feedline, control lines, and qubit capacitance. Josephson junctions are then patterned using e-beam lithography and fabricated through double-angle shadow evaporation of aluminum with in situ oxidation. After lift-off, lithography and deposition of patch establish galvanic connections. Finally, air bridges are added over coplanar waveguide (CPW) structures using optical lithography, aluminum deposition, and etching, to suppress slot-line modes. More details can be found in Ref.^{39,40}.

We use a Qblox cluster as the primary control hardware. It consists of QCM-RF, QRM-RF, and QCM modules. QCM-RF controls the single-qubit gates via the XY drive line of the qubit. QRM-RF is a multiplexed readout module that has two ports, one for sending the readout pulse and another to digitize the received readout signal. It is connected to the IN and OUT lines of the readout. QCM is a control module that can send arbitrary pulses from DC to 400 MHz. It is used on the Z_{AC} line to send flux pulses to the coupler. We also use a Qblox SPI rack that consists of S4g current source modules.

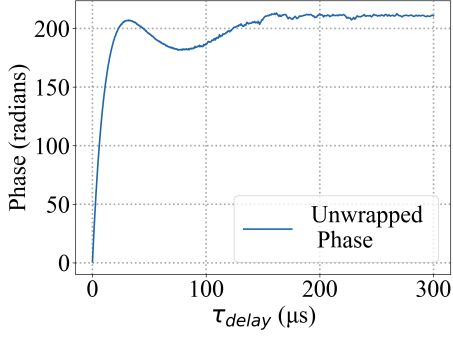


FIG. 6. Extracted unwrapped phase for transients measured with a square pulse of 8 μ s duration as a function of τ_{delay} up to 300 μ s (cf. Fig. 2(e)). The result indicates that the transients do not reach a steady state until after approximately 150 μ s.

It is connected to Z_{DC} and is used to set the static magnetic flux bias on the coupler. The Z_{DC} and Z_{AC} controls of the flux are coupled together with a bias-tee (Marki- BT0025) at room temperature. Measurements are performed utilizing the software suite 'Superconducting Qubit Tools (SCQT)' from Orange Quantum Systems.

Appendix B: Transient measurements up to 300 μ s

In Section II of the main text, we show the measured transients up to 60 μ s, where we fit an exponential decay to estimate the decay constant τ , later related to the equivalent RC constant. Figure 6 shows the measurement of transients up to 300 μ s, revealing that transients do not reach a steady state until after approximately 150 μ s. This indicates that our choice of an exponential fit provides only an approximation to capture the dominant effect, and additional long-time transient effects are not fully accounted for in our first-order model.

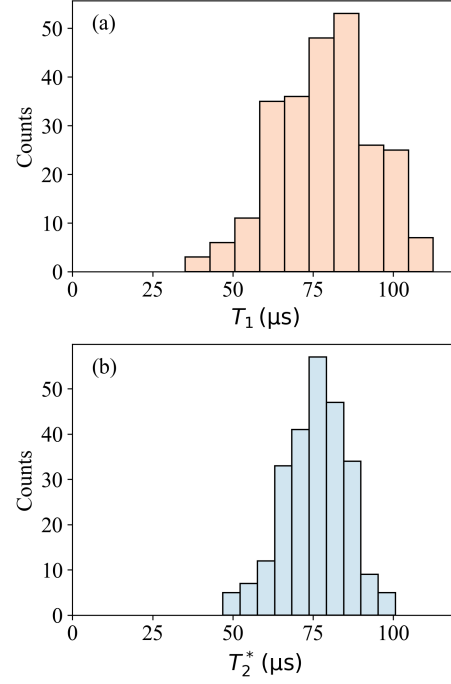


FIG. 7. Histogram distribution of (a) the T_1 relaxation time and (b) the T_2^* free-induction decay (Ramsey) decoherence time of qubit Q1, measured over 8 hours.

Appendix C: Coherence data of Qubit 1

To statistically analyze the relaxation time (T_1) and Ramsey decoherence time (T_2^*) of the qubit Q1, 250 measurements of each were taken over eight hours. The resulting histograms are shown in Fig. 7.

Appendix D: Qubit spectroscopy as a function of flux bias

The device consists of qubit Q1 coupled to a flux-tunable coupler as shown in Fig. 2(a). The coupler's transition frequency is modulated by the magnetic

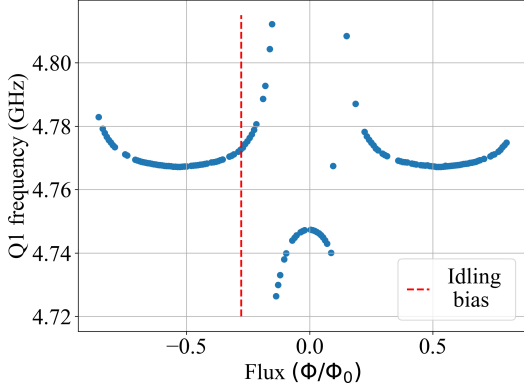


FIG. 8. Frequency of qubit Q1 as a function of the coupler's flux bias. The red dashed line shows the idling coupler bias used in the measurements.

flux threading its SQUID and is given by

$$\omega_c = \omega_{max} \sqrt{|\cos(\pi\Phi/\Phi_0)|}, \quad (D1)$$

where ω_{max} is the coupler's frequency at zero effective bias, and Φ_0 is the magnetic flux quantum.

Tuning the coupler's frequency results in a change of Q1 frequency due to the interaction between qubit and coupler. Figure 8 shows the frequency of Q1 as a function of the coupler flux Φ . When the coupler is far from resonance with the qubit ($\Phi \approx 0.5\Phi_0$), the frequency of Q1 remains nearly constant. However, as the coupler approaches the transition frequency of Q1, an avoided crossing occurs, causing a significant frequency shift. This avoided-crossing region is leveraged in transient measurements to enhance sensitivity. The red dashed line in the plot marks the coupler's bias point during idling.

Appendix E: Single-shot readout fidelity

Transient characterization is performed using single-shot measurements, with state discrimination between the ground, first excited, and second excited states, $|g\rangle$, $|e\rangle$, $|f\rangle$. The measured readout con-

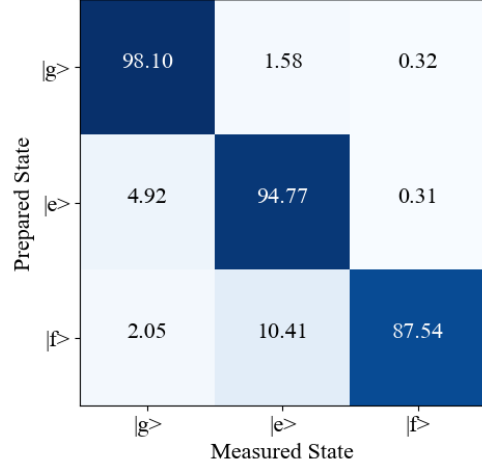


FIG. 9. Readout confusion matrix for Q1. The readout fidelity is about 93.47%.

fusion matrix for qubit Q1 is depicted in Fig. 9. The readout fidelity is approximately 93.47%.

Appendix F: Pulse reconstruction

To verify that the desired pulse shape is reaching the coupler on the chip, we used the cryoscope technique¹⁷. We test the bi-harmonic flux pulse from Eq. (9), with $b_1 = 1$, b_2 extracted from Eq. (12), $m = 100$, and $\tau = 11.2 \mu s$. Figure 10 shows that the expected and measured pulse shapes are in good agreement, except for some regions on the negative side. This occurs because, for a bipolar pulse, accurately capturing both positive and negative amplitudes requires the signal-to-noise ratio (SNR) to be comparable on both sides. In our case, the SNR is higher on the positive side and lower on the negative side. As a result, the negative side is smoothed out during averaging and filtering. One can optimize the idling bias to obtain similar SNR on both sides. In these measurements, the idling coupler bias is at $\Phi = -0.227\Phi_0$.

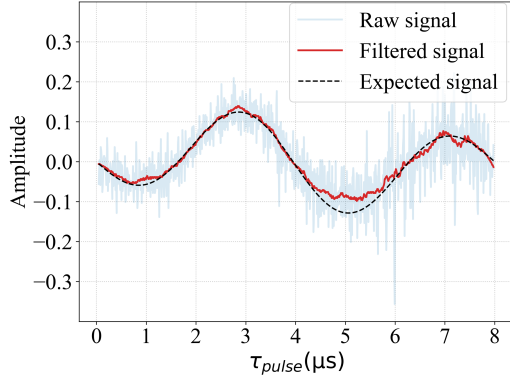


FIG. 10. Pulse reconstruction for a bi-harmonic sine pulse with $m = 100$, $\tau = 11.2 \mu s$, $b_1 = 1$, and b_2 given by Eq. (12). The reconstruction is performed with the cryoscope technique¹⁷.

Appendix G: Network simulations of flux control wiring

To verify our choice of an effective RC model for flux control wiring, we perform network simulations using the Advanced Design System (ADS) software⁴¹. In these simulations, we include components such as attenuators, the capacitor of the bias-tee, a low-pass filter, the inductance from the wirebond (1 nH), the CPW line on-chip, and the inductive coupling of the flux line to the qubit, replicating the actual measurement setup, as shown in Fig. 11(a). We then extend our model by incorporating the 10 foot coaxial cable connecting the bias-tee to the input of the dilution refrigerator, as shown in Fig. 11(b). To accurately model both the low-pass filter and the coaxial cable, we measure their S-parameters and incorporate them into an S2P model in ADS.

Figure 11(c) shows the magnitude of the input impedance $Z_{in,1}$ as a function of frequency, comparing cases with and without the coaxial cable. Without the coaxial cable, the input impedance follows an equivalent RC behavior, with negligible effects from inductors. However, when the coaxial cable is included in the model, oscillations in the in-

put impedance appear at frequencies above approximately 1 MHz. These oscillations arise due to the formation of standing waves caused by impedance mismatches at the connectors.

Appendix H: Fitting method for transients

In Fig. 2(h), we fit the flux transients curve using a fitting function with two exponential terms:

$$A(-e^{-\tau_{\text{delay}}/\tau} + e^{-(\tau_{\text{delay}} + \tau_{\text{pulse}})/\tau}) + B. \quad (\text{H1})$$

The origin of the Eq. (H1) is due to the fact that any any square-shaped pulse $x(t)$ of duration t_0 can be represented as

$$x(t) = x_0(\theta(t) - \theta(t - t_0)), \quad (\text{H2})$$

where $\theta(t)$ is the Heaviside theta function, x_0 is its amplitude. To model the high-pass filter response of the flux signal, we need to convolute $x(t)$ with the $h(t) = e^{-t/\tau}\theta(t)$, resulting in a transient response modeled by two exponential terms.

Appendix I: Phase histogram data

In Table III, we report the extracted mean and standard deviation of the histograms in Fig. 3(d) showing that the mean values for $m = 1, 10, 100$ lie within the standard deviation of the zero (reference) case.

¹R. Acharya, L. Aghababaie-Beni, I. Aleiner, T. I. Andersen, M. Ansmann, F. Arute, K. Arya, A. Asfaw, N. Astrakhantsev, J. Atalaya, *et al.*, “Quantum error correction below the surface code threshold,” arXiv preprint arXiv:2408.13687 (2024).

²S. Krinner, N. Lacroix, A. Remm, A. Di Paolo, E. Genois, C. Leroux, C. Hellings, S. Lazar, F. Swiadek, J. Herrmann, *et al.*, “Realizing repeated quantum error correction in a distance-three surface code,” *Nature* **605**, 669–674 (2022).

³P. Jurcevic, A. Javadi-Abhari, L. S. Bishop, I. Lauer, D. F. Bogorin, M. Brink, L. Capelluto, O. Günlük, T. Itoko, N. Kanazawa, *et al.*, “Demonstration of quantum volume 64

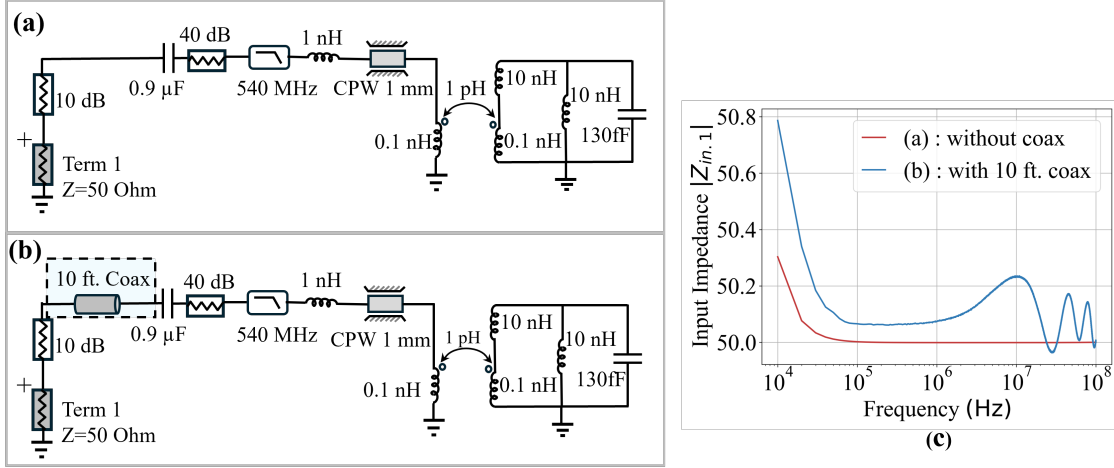


FIG. 11. Network simulations for flux control wiring using Advanced Design System (ADS). (a) Flux control wiring in our setup without considering coaxial cables. (b) Flux control wiring including 10 foot coaxial cable. (c) Simulated input impedance magnitude $|Z_{in,1}|$ for (a) and (b) as a function of frequency.

Type	Mean	Standard-deviation
$m = 1$	-0.006 ± 0.006	0.329 ± 0.004
$m = 10$	0.002 ± 0.011	0.618 ± 0.008
$m = 100$	-0.021 ± 0.005	0.254 ± 0.003
Zero	-0.098 ± 0.004	0.231 ± 0.003

TABLE III. Mean and standard deviation of the histograms in Fig. 3(d).

on a superconducting quantum computing system,” *Quantum Science and Technology* **6**, 025020 (2021).

⁴S. Kosen, H.-X. Li, M. Rommel, D. Shiri, C. Warren, L. Grönberg, J. Salonen, T. Abad, J. Biznárová, M. Caputo, *et al.*, “Building blocks of a flip-chip integrated superconducting quantum processor,” *Quantum Science and Technology* **7**, 035018 (2022).

⁵J. F. Marques, B. Varbanov, M. Moreira, H. Ali, N. Muthusubramanian, C. Zachariadis, F. Battistel, M. Beekman, N. Haider, W. Vlothuizen, *et al.*, “Logical-qubit operations in an error-detecting surface code,” *Nature Physics* **18**, 80–86 (2022).

⁶Y. Zhao, Y. Ye, H.-L. Huang, Y. Zhang, D. Wu, H. Guan, Q. Zhu, Z. Wei, T. He, S. Cao, *et al.*, “Realization of an error-correcting surface code with superconducting qubits,” *Physical Review Letters* **129**, 030501 (2022).

⁷B. Foxen, C. Neill, A. Dunsworth, P. Roushan, B. Chiaro, A. Megrant, J. Kelly, Z. Chen, K. Satzinger, R. Barends, *et al.*, “Demonstrating a continuous set of two-qubit gates for near-term quantum algorithms,” *Physical Review Letters* **125**,

120504 (2020).

⁸M. Rol, F. Battistel, F. Malinowski, C. Bultink, B. Tarasinski, R. Vollmer, N. Haider, N. Muthusubramanian, A. Bruno, B. Terhal, *et al.*, “A fast, low-leakage, high-fidelity two-qubit gate for a programmable superconducting quantum computer,” *arXiv preprint arXiv:1903.02492* (2019).

⁹F. Marxer, A. Vepsäläinen, S. W. Jolin, J. Tuorila, A. Landra, C. Ockeloen-Korppi, W. Liu, O. Ahonen, A. Auer, L. Belzane, *et al.*, “Long-distance transmon coupler with cz-gate fidelity above 99.8%,” *PRX Quantum* **4**, 010314 (2023).

¹⁰R. Li, K. Kubo, Y. Ho, Z. Yan, Y. Nakamura, and H. Goto, “Realization of high-fidelity cz gate based on a double-transmon coupler,” *Physical Review X* **14**, 041050 (2024).

¹¹Y. Xu, J. Chu, J. Yuan, J. Qiu, Y. Zhou, L. Zhang, X. Tan, Y. Yu, S. Liu, J. Li, *et al.*, “High-fidelity, high-scalability two-qubit gate scheme for superconducting qubits,” *Physical review letters* **125**, 240503 (2020).

¹²M. D. Reed, B. R. Johnson, A. A. Houck, L. DiCarlo, J. M. Chow, D. I. Schuster, L. Frunzio, and R. J. Schoelkopf, “Fast reset and suppressing spontaneous emission of a superconducting qubit,” *Applied Physics Letters* **96** (2010).

¹³L. Chen, S. P. Fors, Z. Yan, A. Ali, T. Abad, A. Osman, E. Moschandreou, B. Lienhard, S. Kosen, H.-X. Li, *et al.*, “Fast unconditional reset and leakage reduction in fixed-frequency transmon qubits,” *arXiv preprint arXiv:2409.16748* (2024).

¹⁴X. Yang, J. Chu, Z. Guo, W. Huang, Y. Liang, J. Liu, J. Qiu, X. Sun, Z. Tao, J. Zhang, *et al.*, “Coupler-assisted leakage reduction for scalable quantum error correction with superconducting qubits,” *Physical Review Letters* **133**, 170601 (2024).

¹⁵M. McEwen, D. Kafri, Z. Chen, J. Atalaya, K. Satzinger, C. Quintana, P. V. Klimov, D. Sank, C. Gidney, A. Fowler, *et al.*, “Removing leakage-induced correlated errors in super-

- conducting quantum error correction,” *Nature communications* **12**, 1761 (2021).
- ¹⁶N. Lacroix, L. Hofele, A. Remm, O. Benhayoune-Khadraoui, A. McDonald, R. Shillito, S. Lazar, C. Hellings, F. Swiadek, D. Colao-Zanuz, *et al.*, “Fast flux-activated leakage reduction for superconducting quantum circuits,” *arXiv preprint arXiv:2309.07060* (2023).
 - ¹⁷M. A. Rol, L. Ciorciaro, F. K. Malinowski, B. M. Tarasinski, R. E. Sagastizabal, C. C. Bultink, Y. Salathe, N. Haandbæk, J. Sedivy, and L. DiCarlo, “Time-domain characterization and correction of on-chip distortion of control pulses in a quantum processor,” *Applied Physics Letters* **116** (2020).
 - ¹⁸Y. Sung, L. Ding, J. Braumüller, A. Vepsäläinen, B. Kannan, M. Kjaergaard, A. Greene, G. O. Samach, C. McNally, D. Kim, *et al.*, “Realization of high-fidelity cz and zz-free iswap gates with a tunable coupler,” *Physical Review X* **11**, 021058 (2021).
 - ¹⁹L.-L. Guo, P. Duan, S. Zhang, X.-X. Yang, C. Zhang, L. Du, H.-F. Zhang, H.-R. Tao, T.-L. Wang, Z.-L. Jia, *et al.*, “Universal scalable characterization and correction of pulse distortions in controlled quantum systems,” *Physical Review Applied* **21**, 064060 (2024).
 - ²⁰J. Heinsoo, *Digital quantum computation with superconducting qubits*, Ph.D. thesis, ETH Zurich (2019).
 - ²¹B. R. Johnson, *Controlling photons in superconducting electrical circuits*, Ph.D. thesis, Yale University (2011).
 - ²²M. Baur, *Realizing quantum gates and algorithms with three superconducting qubits*, Ph.D. thesis, ETH Zurich (2012).
 - ²³J. Butscher, *Shaping of Fast Flux Pulses for Two-Qubit Gates: Inverse Filtering*, Master’s thesis, ETH Zürich (2018).
 - ²⁴T.-M. Li, J.-C. Zhang, B.-J. Chen, K. Huang, H.-T. Liu, Y.-X. Xiao, C.-L. Deng, G.-H. Liang, C.-T. Chen, Y. Liu, *et al.*, “High-precision pulse calibration of tunable couplers for high-fidelity two-qubit gates in superconducting quantum processors,” *arXiv preprint arXiv:2410.15041* (2024).
 - ²⁵C. Zhang, T.-L. Wang, L.-L. Guo, X.-Y. Yang, X.-X. Yang, P. Duan, Z.-L. Jia, W.-C. Kong, and G.-P. Guo, “Characterization of tunable coupler without a dedicated readout resonator in superconducting circuits,” *Applied Physics Letters* **122** (2023).
 - ²⁶M. Jerger, A. Kulikov, Z. Vasselin, and A. Fedorov, “In situ characterization of qubit control lines: A qubit as a vector network analyzer,” *Physical review letters* **123**, 150501 (2019).
 - ²⁷X. Zhang, X. Zhang, C. Chen, K. Tang, K. Yi, K. Luo, Z. Xie, Y. Chen, and T. Yan, “Characterization and optimization of tunable couplers via adiabatic control in superconducting circuits,” *arXiv preprint arXiv:2501.13646* (2025).
 - ²⁸B. Foxen, J. Mutus, E. Lucero, E. Jeffrey, D. Sank, R. Barends, K. Arya, B. Burkett, Y. Chen, Z. Chen, *et al.*, “High speed flux sampling for tunable superconducting qubits with an embedded cryogenic transducer,” *Superconductor Science and Technology* **32**, 015012 (2018).
 - ²⁹A. V. Oppenheim, A. S. Willsky, and S. H. Nawab, *Signals & systems* (Pearson Educación, 1997).
 - ³⁰SciPy, “scipy savgol filter,” (2024).
 - ³¹J. Koch, T. M. Yu, J. Gambetta, A. A. Houck, D. I. Schuster, J. Majer, A. Blais, M. H. Devoret, S. M. Girvin, and R. J. Schoelkopf, “Charge-insensitive qubit design derived from the cooper pair box,” *Physical Review A—Atomic, Molecular, and Optical Physics* **76**, 042319 (2007).
 - ³²A. Bengtsson, P. Vikstål, C. Warren, M. Svensson, X. Gu, A. F. Kockum, P. Krantz, C. Križan, D. Shiri, I.-M. Svensson, *et al.*, “Improved success probability with greater circuit depth for the quantum approximate optimization algorithm,” *Physical Review Applied* **14**, 034010 (2020).
 - ³³D. C. McKay, S. Filipp, A. Mezzacapo, E. Magesan, J. M. Chow, and J. M. Gambetta, “Universal gate for fixed-frequency qubits via a tunable bus,” *Physical Review Applied* **6**, 064007 (2016).
 - ³⁴N. J. Glaser, F. A. Roy, I. Tsitsilin, L. Koch, N. Bruckmoser, J. Schirk, J. H. Romeiro, G. B. Huber, F. Wallner, M. Singh, *et al.*, “Sensitivity-adapted closed-loop optimization for high-fidelity controlled-z gates in superconducting qubits,” *arXiv preprint arXiv:2412.17454* (2024).
 - ³⁵J. Wenner, M. Neeley, R. C. Bialczak, M. Lenander, E. Lucero, A. D. O’Connell, D. Sank, H. Wang, M. Weides, A. N. Cleland, *et al.*, “Wirebond crosstalk and cavity modes in large chip mounts for superconducting qubits,” *Superconductor Science and Technology* **24**, 065001 (2011).
 - ³⁶H.-X. LI, “Flip-chip integrated superconducting quantum processors,” (2025).
 - ³⁷Since our model is a series RC circuit, any transients in the voltage across the capacitor (V_c) translate into transients in the current as $I = C \frac{dV_c(t)}{dt}$.
 - ³⁸R. Rehammar and S. Gasparinetti, “Low-pass filter with ultrawide stopband for quantum computing applications,” *IEEE Transactions on Microwave Theory and Techniques* **71**, 3075–3080 (2023).
 - ³⁹J. Biznárová, A. Osman, E. Rehnman, L. Chayanun, C. Križan, P. Malmberg, M. Rommel, C. Warren, P. Delsing, A. Yurgens, *et al.*, “Mitigation of interfacial dielectric loss in aluminum-on-silicon superconducting qubits,” *npj Quantum Information* **10**, 78 (2024).
 - ⁴⁰L. Chayanun, J. Biznárová, L. Zeng, P. Malmberg, A. Nylander, A. Osman, M. Rommel, P. L. Tam, E. Olsson, P. Delsing, *et al.*, “Characterization of process-related interfacial dielectric loss in aluminum-on-silicon by resonator microwave measurements, materials analysis, and imaging,” *APL Quantum* **1** (2024).
 - ⁴¹Keysight, “Advanced Design System (ADS),” (2023).